A Physics-based Model Assisted by Machine-Learning for Sodium-ion Batteries with both Liquid and Solid Electrolytes

Journal of The Electrochemical Society, 2024 **171** 060516
1945-7111/2024/171(6)/060516/10/$40.00 © 2024 The Electrochemical Society ("ECS"). Published on behalf of ECS by IOP Publishing Limited

A Physics-based Model Assisted by Machine-Learning for Sodium-ion Batteries with both Liquid and Solid Electrolytes

Harsh Dilipkumar Jagad,[1] Jintao Fu,[2] William R. Fullerton,[3] Christopher Y. Li,[3] Eric Detsi,[2] and Yue Qi[1,*,z]

[1]*School of Engineering, Brown University, Providence Rhode Island 02906, United States of America*
[2]*Department of Materials Science and Engineering, University of Pennsylvania, Philadelphia Pennsylvania 19104, United States of America*
[3]*Department of Materials Science and Engineering, Drexel University, Philadelphia Pennsylvania 19104, United States of America*

In the absence of experimental data of fully developed hierarchical 3D sodium solid-state batteries, we developed an improved continuum model by relying on Machine Learning-assisted parameter fitting to uncover the intrinsic material properties that can be transferred into different battery models. The electrochemical system simulated has sodium metal P2-type $Na_{2/3}[Ni_{1/3}Fe_{1/12}Mn_{7/12}]O_2$ (NNFMO) as the cathode material, paired with two types of electrolytes viz, the organic liquid electrolyte and a solid polymer electrolyte. We implemented a 1D continuum model in COMSOL to suit both liquid and solid electrolytes, then used a Gaussian Process Regressor to fit and evaluate the electrochemical parameters in both battery systems. To enhance the generalizability of our model, the liquid cell and solid cell models share the same OCV input for the cathode materials. The resulting parameters are well aligned with their physical meaning and literature values. The continuum model is then used to understand the effect of increasing the thickness of the cathode and current density by analyzing the cathode utilization, and the overpotentials arising from transport and charge transfer. This 1D model and the parameter set are ready to be used in a 3D battery architecture design.
 [DOI: 10.1149/1945-7111/ad4a11]

Manuscript submitted March 19, 2024; revised manuscript received April 28, 2024. Published June 11, 2024.

Supplementary material for this article is available online

Three-dimensional (3D) solid-state batteries have been proposed by Long et al. in 2004 as an architecture to minimize diffusion length in traditional porous electrodes, thus simultaneously increasing energy and power densities.[1–3] However, its manufacturing and integration process has been a challenge. Various methods, such as vapor deposition techniques,[4,5] laser creation of diffusion channels,[6,7] and freeze casting[8,9] have been explored, along with other methods considering manufacturing scalability. The geometry of 3D batteries, such as the shape and thickness of the active material and the electrolyte is a subject of design for active material utilization and energy and power densities. For example, the optimal spatial thickness of electrodes was investigated based on the Faradaic specific energy density of the battery by McClosky.[10] Pearse et al. optimized the spatial thickness by defining the increase in the reaction interface area in a patterned 3D vs planar geometry.[3] Increasing the reaction interface in the same volume reduced the diffusional length for the Li^+ and led to higher utilization of the active material. Heubner et al. defined a limiting thickness of the electrode as the thickness that does not have Li intercalating at the far end of the electrode for a given current density due to diffusion limitation.[11] Weiss et al. discussed an optimal ratio of the thickness of the electrode and electrolyte in relation to the current density and the transport based overpotentials.[12] In this work, we will explore the design of the optimal thickness of the electrode in relation to the utilization of the active material, current density, and the resulting overpotentials.

A continuum scale solid state battery model can guide and accelerate this design process.[13–15] Mechanistic driven continuum models offer the possibility to delineate the contributions of various phenomena towards the performance of batteries, for example, diffusional transport, electrochemical reactions, and their coupling, etc. The mechanism based models can be traced to the pseudo particle 2D models (P2D),[16,17] single particle models (SPM),[18–20] or simple 1D thin film models.[13,14,21] The P2D models were developed to simulate the porous electrodes and optimize the energy and power density of the battery. The SPM models assume a solid phase for the electrode without any electrolyte phase and have been used to investigate the thermal behavior of batteries. These models have provided insights into diffusion induced stress in the electrodes[22] and the rate performance of cathodes.[15] The simple 1D thin film based models, assuming fully dense phases for the electrode and electrolyte, have been used to simulate contact area loss in solid state batteries[14] and are more appropriate to serve as the base for 3D all solid state battery modeling.[21] Regardless of the type of model and the phenomenon being investigated, continuum models depend on the choice of parameters used as input. Thus, the accuracy of the model depends relatively on the values used for the parameters.

The input parameters for continuum models have been well documented and utilized for lithium-ion batteries especially employing liquid electrolytes or solid polymer electrolytes (SPE).[15–17,23] Due to the geo-political nature of lithium-ion batteries, there is an increasing focus to transition to the cheaper and more accessible sodium-ion batteries.[24–26] However, the literature reporting the electrochemical modeling parameters for sodium-ion batteries is much less than that in lithium-ion batteries especially when SPE is used. Thus, obtaining intrinsic material parameters that can be transferred to other battery models is the main focus of this paper.

Typically, the parameters used in continuum modeling are obtained from experiments or predictive modeling. Individual parameters like the diffusivity and rate constants can be investigated at the atomic or molecular dynamics scale.[27] If rich experimental data is available, the input parameters for the continuum model can be estimated using normalization and sensitivity analysis,[28,29] Bayesian estimation,[30] and Gaussian Process Regression (GPR)[31] based on experimental input. A natural question then arises, how to obtain the parameters, especially in a battery (e.g. 3D hierarchical solid-state sodium battery) that has not been experimentally developed yet? One way to address this challenge is to obtain intrinsic material and interfacial properties that remain unchanged based on the architecture of the battery. For example, the solid-state diffusivity of a cathode material is a property unique to the material, and similarly, the interfacial electrolyte | electrode charge transfer rate constant does not vary with architecture. Thus, we obtain these

*Electrochemical Society Member.
[z]E-mail: yueqi@brown.edu

material parameters from the simplest 1D experiments. We show that minimal coin cell level experiments, paired with a 1D continuum scale model can be used to obtain these parameters using a surrogate model-based Machine Learning (ML) method.

A surrogate model can approximate the behavior of an original complex model and is less resource intensive to compute.[32,33] Hence they have been used to model coupled complex phenomena with battery performance, e.g. the state of charge[34] and Ragone plot.[35] Surrogate models are especially useful when experimental data is scarce. For example, Yu et al. also used surrogate models to obtain parameters like diffusivity, rate constants, and transference number by fitting the voltage vs time plots.[36] The accuracy of the different algorithms for parameter optimization in surrogate models has been reported recently.[37] Inspired by these models we use a surrogate model to optimize the electrochemical parameters for our continuum model.

The continuum model using the validated parameters is then used to analyze the utilization rate of the cathode and the overpotentials generated due to mass transport in the solid polymer electrolyte, cathode, and the charge transfer reactions at the interfaces. Analytical relationships linking the current density and the thickness of the cathode to the utilization, and the overpotentials are provided. The major overpotential is found to be linked to the charge transfer at the interfaces. Correspondingly current densities and cathode thickness' that cause a 10% drop in the energy density of the cathode are estimated from the charge transfer overpotential.

Model

1D model overview.—The electrochemical discharge performance of the Na anode coupled with the NNFMO cathode was modeled using a 1D continuum model, a schematic is shown in Fig. 1.

Model geometry.—**Anode:** The anode is assumed as an infinite source of Na^+ ions, which is reasonable because the electrode loading ratio (anode capacity/cathode capacity) in typical batteries is always >1 and the metallic Na anode does not have electron transport limitations. Hence, the thickness of the anode is not included in the current model.

Cathode: Although the current experiments were performed with a porous active cathode material, we treated it as a monolithic block, i.e. one without pores or microstructure, albeit with a reduced thickness. This is justified because the experimental cathode is extremely porous (further details in the experimental section). The diffusion of Na in the cathode is almost an order of magnitude slower[38,39] than the diffusion of the mobile Na^+ in both the liquid[40–42] and SPE.[43,44] This allows us to use the 1D continuum model by discounting the experimental binder, conductive agent, porosity, and all other non-active components (which do not contribute to solid state diffusion in the cathode) into a reduced dimensional model which is based purely on the slowest solid state diffusion in the cathode. The thickness of the single monolithic block is comparable to the traditional electrode particle size in experiments. Hence, the concentration of Na in the cathode of the 1D model is equal to the theoretical concentration of Na in $Na_{0.66}NFMO$.[45]

Electrolyte: Two types of electrolytes are considered viz, SPE and liquid electrolyte. Although some of the experimental thickness of the liquid electrolyte separator is 260 microns, it is estimated that a negligible voltage drop on the order of 0.02 V at 10 C (12.5 A/m^2) given a typical ionic conductivity of 10^{-3} S/cm of liquid electrolyte. Therefore, the length of the electrolyte, L, is set to 35 microns for both electrolytes, close to the experimental SPE value and commercially available separators.[46] In the 1D model, we also assume a contact area fraction, γ, at the electrolyte|cathode interface and a conformal interface between the anode and the electrolyte. This is explicitly evaluated for the SPE and assumed to be 1 for liquid electrolytes.

The model can thus be broken down into the following components, the anode|electrolyte interface, the core electrolyte region, the electrolyte|cathode interface node, and the cathode slab.

1D model transport equations.— *Anode|electrolyte interface.*— The charge transfer process between the Na-metal (from the anode) and the Na^+ ions results in the creation of Na^+ at the interface.

$$Na^0 \leftrightarrow Na^+ + e^- \tag{1}$$

The charge transfer reaction at the anode interface is modeled using the standard Butler-Volmer equation, which gives the net current density at the anode (i_{anode}):

$$i_{anode} = Fk_{neg}\left(\frac{C^+_{Na}}{C^+_{Na_0}}\right)^{\alpha_{anode}}\left(e^{\frac{\alpha_{anode}F\eta^{anode}_{ct}}{RT}} - e^{\frac{-(1-\alpha_{anode})F\eta^{anode}_{ct}}{RT}}\right) \tag{1}$$

Where F is the Faraday's constant, k_{neg} is the rate of the charge transfer reaction, α_{anode} is the charge transfer coefficient at the anode|electrolyte interface, R is the gas constant, T is temperature, η^{anode}_{ct} is the charge transfer overpotential at the anode|electrolyte interface and is defined as the difference between the external electric

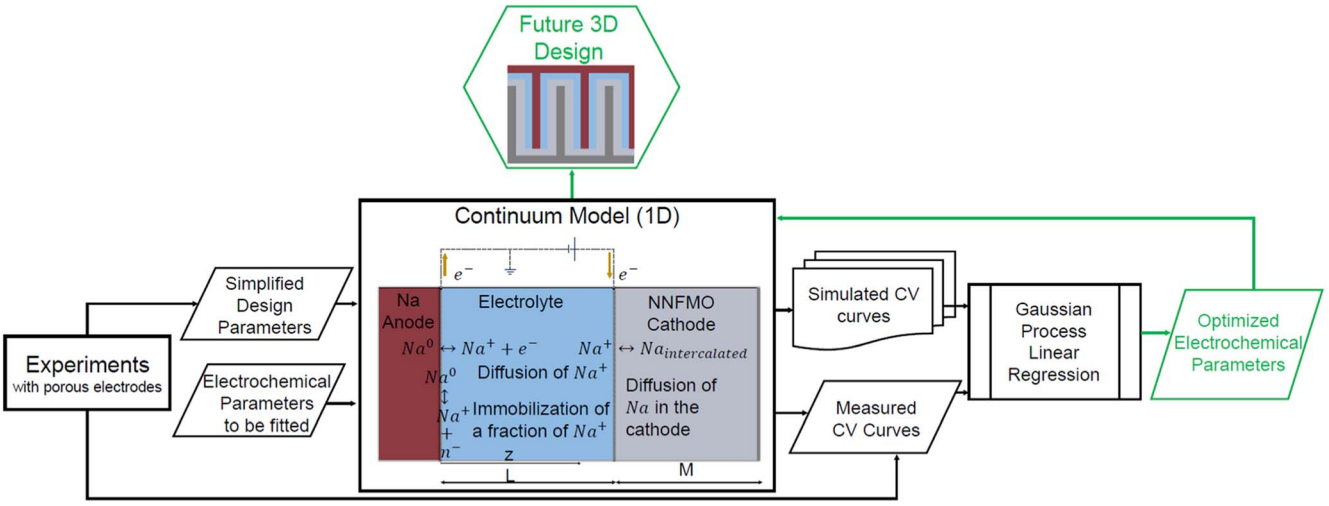

Figure 1. Schematic showing the process of developing a hierarchical 3D battery model by combining the use of porous electrode experiments, a 1D continuum model, and a surrogate model. The continuum model contains the anode (red), anode|electrolyte interface, the electrolyte (blue; thickness L), the electrolyte|cathode interface, and the cathode region (grey, thickness M).

potential in the electrode ϕ_{anode} (set to zero) and the electrolyte ϕ_{el} with respect to the equilibrium potential E_{eq} (zero for Na metallic state).

Electrolyte.—Various models exist to describe cation transport in electrolytes[13,14,16,47] including solid inorganic electrolytes, SPE, and polymer-separator filled with liquid electrolytes. Generally, all ions are mobile in liquid electrolytes and the transfer number is close to 0.5.[40,48] However, there is a limiting concentration of mobile Li^+ in solid electrolytes.[13,14] Here we adopted one model for both liquid and solid electrolytes, following Refs. 14 and 13 .

While most of the Na^+ ions are considered mobile in the liquid electrolyte, it is assumed that not all the Na^+ ions in the SPE are mobile i.e., there exists an equilibrium fraction of Na^+ that is immobile as they are strongly bonded by negatively charged species, n^-. This is inspired by the model developed by Sequeira and Hooper for polymer electrolytes containing a Li^+ salt[49] and implemented widely in solid electrolytes having a dilute concentration of cations.[13,14,21,50,51] Sequeira and Hooper showed this model holds in the dilute limit (repeating unit/Li ratio > 10),[49] which is the case for the SPE in our experiments. It also describes the non-ideal solution model when salt concentration is below 1 M in liquid electrolyte.[52] It was discussed that when the salt concentration in the polymer electrolyte is higher (repeating unit/Li ratio < 9), an explicit correction incorporating the activity and fugacity must be employed. It is shown in later discussions that the dilute assumption holds up to a 2 C rate in the solid electrolyte.

In this model, an equilibrium fraction δ is defined as the ratio of the mobile cations, C^+_{Na}, with the total number of cations available in the electrolyte, $C^+_{Na_t}$. The reaction is written as:

$$Na^0_{immmobile} \leftrightarrow Na^+_{mobile} + n^- \tag{1}$$

The rate of the generation of mobile Na^+, r, is expressed in terms of the rate constants, (k_r, k_d), and the concentration of the charge compensating species C^-_n:

$$r = k_d C_{immobile} - k_r C^+_{Na} C^-_n \tag{2}$$

At equilibrium, the forward and backward rates are equal thus:

$$k_d C_{immobile} = k_r C^+_{Na} C^-_n$$

$$k_d C_{Na_t}{}^+(1-\delta) = k_r C_{Na_t}{}^+\delta \cdot C_{Na_t}{}^+\delta$$

$$r = k_r[C_{Na_t}{}^{+2}\delta^2 - C^{+\,2}_{Na}] \tag{3}$$

In the case of liquid electrolyte, we use an equilibrium fraction of 0.9 which implies that virtually all the Na^+ is mobile. The δ may be lowered to values of ~0.18 as done by[13,14] for the case of LiPON. Based on the experimental data for PEO, we choose $\delta = 0.12$ for the case of the SPE in our study.

For both electrolytes, the transport of Na^+ and charge conserving negative species, n^-, are considered. No convection currents are included. Their diffusion processes are governed by the Nernst-Planck equation coupled with Fick's second law.

$$\frac{\partial C_i}{\partial t} = -\nabla J_i + r \tag{4}$$

where t is the time, r is the rate of generation (source/sink) of mobile species (Eqs. 2 and 3) and J_i is the flux of the mobile species (Na^+, n^-) given by:

$$J_i = -\nabla D_i C_i + \frac{qF}{RT} D_i C_i \nabla\phi_{el} \tag{5}$$

where D_i is the diffusion of the mobile species (Na^+, n^-) in the electrolyte, q is the charge $= +1$ for Na^+ and -1 for n^-, $\nabla\phi_{el}$ is the gradient in the electrical potential.

The diffusion coefficient of the negative species (D^-_n) and the positive species (D^+_{Na}) is related via the transfer number, t^+ in the electrolytes, as $D^-_n = \frac{D^+_{Na}(1-t^+)}{t^+}$. D^+_{Na} will be fitted to experimental values, while D^-_n is calculated based on $t^+ = 0.42$. The experimental values of t^+ in the SPE measured by the Bruce Vincent method yielded 0.42, which is in line with the typical value of 0.3–0.5 reported for a dilute Na salt concentration in a polymer matrix.[53,54] It is also a reasonable assumption for liquid electrolytes taken from literature.[55,56] It can be shown that writing Eq. 4 for the two species and holding the electroneutrality condition reduces Eq. 4 for C^+_{Na} as

$$\frac{\partial C^+_{Na}}{\partial t} = (2D^+_{Na}(1-t^+))\frac{\partial^2 C^+_{Na}}{\partial z^2} + r \tag{6}$$

Thus C^+_{Na} depending explicitly on the transference number, as shown in Ref. 13.

Electrolyte|cathode interface.—At the electrolyte|NNFMO cathode interface, there is a corresponding charge transfer reaction which is modeled using the Butler-Volmer equation:

$$Na_0NFMO + xNa^+ + xe^- \leftrightarrow Na_xNFMO$$

$$i_{cathode} = F\gamma k_{pos}\left(\frac{(C^s_{Na|\max} - C^s_{Na})C^+_{Na}}{(C^s_{Na|\max} - C^s_{Na|\min})C^+_{Na_0}}\right)^{\alpha_{cathode}} \left(\frac{(C^s_{Na} - C^s_{Na|\min})}{(C^s_{Na|\max} - C^s_{Na|\min})}\right)^{1-\alpha_{cathode}} \left(e^{\frac{\alpha_{cathode}F\eta^{cathode}_{ct}}{RT}} - e^{\frac{-(1-\alpha_{cathode})F\eta^{cathode}_{ct}}{RT}}\right) \tag{7}$$

where k_{pos} is the rate of the charge transfer reaction at the cathode interface, $C^s_{Na|\max}$ is the maximum concentration of the intercalated Na^+ ions in the cathode (corresponding to x = 0.66) and $C^s_{Na|\min}$ is the minimum concentration of Na^+ in the cathode (corresponding to x = 0.33). $\alpha_{cathode}$ is the Butler Volmer charge transfer coefficient at the cathode interface. The $\eta^{cathode}_{ct}$ at the cathode interface corresponds to the charge transfer overpotential at the electrolyte|cathode interface.

$$\eta^{cathode}_{ct} = \phi_{cathode} - \phi_{el} - E_{eq} \tag{8}$$

$\phi_{cathode}$ is the external electrical potential of the cathode (set to 4 V vs Na^+/Na at the beginning of discharge), and E_{eq} refers to the Open Circuit Voltage (OCV) of the cathode with respect to the Na/Na^+ anode.

Another difference between liquid and solid electrolyte is the interfacial contact area. A liquid electrolyte can infiltrate the pores of the porous cathode. A near 100% pore infiltration is assumed by setting the contact area fraction between the cathode and the electrolyte to 1. On the other hand, this is not true for the case of polymer, cathode composite material. The contact area fraction, γ, is implemented as discussed in Ref. 14. The imperfect contact area corrections are made to two equations (Eq. 7 and boundary condition for Eq. 9, shown in SI). First, the cathode current density is scaled with the contact area, second, the rate of generation of Na in the cathode is scaled with the contact area.[14]

Cathode.—The transport within the cathode is driven by a concentration gradient of Na and is written as:

$$\frac{\partial C_{Na}^{s}}{\partial t} = -\nabla(D_{Na}^{s}\ \nabla C_{Na}^{s}) \quad [9]$$

where D_{Na}^{s} is the diffusion coefficient of Na in the NNFMO cathode fitted to experiments.

To summarize, the model solves the coupled differential equations for C_{Na}^{+}, C_{n}^{-}, C_{Na}^{S} and $\phi_{cathode}$, ϕ_{el}. The boundary conditions and the initial conditions are listed in SI.

Open circuit voltage (OCV) for the cathode.—The 0.2 C experimental discharge curve when using the liquid electrolyte was taken as the equilibrium voltage profile for the NNFMO cathode between 4–2 V vs Na^{+}/Na. This is acceptable because the discharge process at a C rate of 0.2 C is slow and hence approximates the equilibrium discharge OCV. The voltage range was chosen to prevent the rapid cyclic capacity loss reported for the NNMO system during high voltage discharge.[57–59] Following the works of[60] and,[61] the stoichiometric fraction of x in Na_xNFMO was interpolated between $x_{max} = 0.66$ at 2 V and $x_0 = 0.33$ at 4 V. Thus, the moles of Na^{+} that get deintercalated from the cathode are $0.66 \sim 0.33$. The molecular weight used (M_w) = 103.59 g for x = 0.66.

Fitting procedure for materials and interface properties.—The set of electrochemical parameters: diffusion coefficient of Na^{+} in electrolyte (D_{Na}^{+}), diffusion of Na in the cathode (D_{Na}^{s}), reaction rate constant on the positive (k_{pos}) and negative (k_{neg}) electrodes, the recombination rate of mobile/immobile sodium at the anode|electrolyte interface (k_r) are fitted. In the case of polymer electrolytes, the contact area fraction (γ) is fitted in addition.

A unique set of the aforementioned parameters when used as an input in COMSOL,[62] generates an output discharge capacity and voltage curves (CV curve). 50 such curves are generated for the SPE, and 30 for liquid electrolytes using a range of electrochemical parameters. The experimental CV curve is taken as a target curve. The Root Mean Square (RMS) value between the target curve and each of the continuum model CV curves is evaluated. RMS is more sensitive to outliers than Mean Absolute Error (MAE) and less sensitive than Mean Square Error (MSE), thus it is chosen as a compromise of MAE and MSE for the large range of the parameter space. It is to be noted that the RMS is performed on the transpose of the traditional CV curve i.e. the vertical axis is the specific capacity and the horizontal axis is the voltage. This was done because of two main reasons. First, the model and target curves both share the same voltage range. Second, the RMS output can be compared with the theoretical specific capacity which is a fixed number.

The RMS values and the set of electrochemical parameters are then fed to a surrogate model implemented in Scikit.[63] The surrogate model uses a Gaussian Process Linear Regression (GPLR) technique to optimize the parameters in the space of the range of the electrochemical parameters that minimizes the RMS. The space of the parameter search was from the minimum value to the maximum value of each of the parameters. The contact area parameter's space was linearly spaced. For all other parameters, a log uniform spacing was used. A Mattern kernel was used to ensure smoothness with ν set to 2.5 to achieve a surrogate model R^2 score of 0.985. The acquisition function used was the negative expected improvement (EI) function with 100 calls of parameter optimization. The optimal electrochemical parameters are then used as input parameters for the COMSOL model, and the output CV curves are validated against experiments. In addition, the surrogate model was split into a 10-fold test train set (TTS). The RMS of the TTS set is shown in the SI for each of the solid polymer and liquid electrolyte datasets.

Experiments and Parameters

Liquid electrolyte.—The NNFMO active cathode material was developed by solid-state reaction of nanoporous nickel (NP-Ni), sodium permanganate monohydrate ($NaMnO_4{\cdot}H_2O$), and iron nitrate nonahydrate ($Fe(NO_3)_3.9H_2O$). Specifically, NP-Ni was prepared following the previously reported procedure,[64,65] which was mixed with a stoichiometric amount of $NaMnO_4{\cdot}H_2O$ and $Fe(NO_3)_3.9H_2O$. The mixture was then dispersed in 1 ml of 1 M sodium hydroxide (NaOH) solution. The NaOH provided an additional source of Na to compensate for the Na loss during high temperature annealing.[66,67] The dispersion was heated at 150 °C in the air on a hot plate to evaporate water, followed by ball-milling for 1 h. Finally, solid-state conversion was performed at 900 °C for 24 h in air and the product was naturally cooled down to room temperature.

The NNFMO powder was then homogeneously mixed with conductive carbon (equal mass of carbon black, carbon nanofibers, and graphene nanosheets) and binder (40 mg/ml of polyvinylidene fluoride dissolved in N-methyl-2-pyrrolidone) in a mass ratio of 7:2:1 to assemble a slurry. The slurry was cast onto Al foil current collector and dried under vacuum at room temperature overnight, followed by heating at 150 °C under an argon atmosphere for 2 h to remove residual water. After drying, circular electrode disks were cut out with an active material loading of $\approx$1.5 mg/cm^2 with an approximate thickness of 40 microns ($M_{cathode}$).

2032-type coin cells were assembled in an argon-filled glovebox with Na metal foil as the anode and NNFMO slurry electrode as the cathode, with a separator filled with liquid electrolyte in between. Sodium metal cubes (99.9% trace metals basis) were purchased from Sigma Aldrich and sodium foil was made by cutting the cubes into slices and rolling them between two mylar sheets. The liquid electrolyte is made by dissolving 1 M sodium perchlorate ($NaClO_4$) in ethylene carbonate (EC)/dimethyl carbonate (DMC) (1:1 by volume) with 5 vol. % addition of fluoroethylene carbonate (FEC). Glass microfiber filters ordered from Sigma Aldrich was used as the separator which has a thickness of 260 microns and a pore size of 1.2 microns (Whatman® glass microfiber filters). The discharge curves at different rates are shown in SI Fig. S–1.

Polymer electrolyte experimental setup.—Solid polymer electrolyte was synthesized from Poly(glycidyl methacrylate) (PGMA, Mn 10−20 kDa, poly(ethylene glycol)) diamine (PEG, Mn 6 kDa). The monomer solution with PGMA:PEG at 4:1 molar ratio was mixed with NaFSI in a 1:3 volume ratio mixed solvent of tetrahydrofuran (THF) and dimethylformamide (DMF). Then the solution was cast onto a glass slide then heated under vacuum at 90 °C for 24 h and 120 °C for 12 h to ensure complete crosslinking between the epoxide and amine functional groups. The crosslinked SPE films are denoted as 4PGMA−PEG_{6k}, where 4 indicates the molar ratio of PGMA monomer/PEG and 6k refers to the PEG molecular weight. The SPEs maintained a monomer: salt (EO:Na) ratio of 16:1. SPE film thickness was between 30–35 microns.

The method to synthesize NNFMO is the same as the Liquid Electrolyte Experimental setup. NNFMO composite cathodes were prepared by mixing NNFMO, the 4PGMA-PEG_{6k} SPE monomers, and super P at a weight ratio of 56/12/32 with N-Methyl-2-pyrrolidone (NMP) at a solvent to cathode volume ratio of 3:1. The slurry was bath sonicated for a total of 3 h, with intermittent mixing using magnetic stirring every 20 min. Following the mixing process, the slurry was coated onto the aluminium foil with an active mass loading (m_l) of 3 mg/cm^2 using a doctor blade, and subsequently dried and polymerized under vacuum at 120 °C for 16 h. The cathode was then calendared using a rolling press. After calendaring, the cathode was dried for an additional 16 h at 120 °C to remove any residual NMP. The final thickness of the composite electrode was between 30–35 microns ($M_{cathode}$). The fully dense monolithic cathode length is calculated based on the active mass loading, as $M = \frac{m_l x_{max}}{M_w C_{Na|max}^{s}} = 7.43$ microns. Hence, the active volume fraction (V_{active}) is $V_{active} = \frac{M}{M\_cathode} \sim 23\%$.

Na|SPE|NNFMO cells were assembled in the glovebox using 2032-coin cell cases. Na metal cubes (99.9% trace metals basis)

Table 1. List of physical parameters used in the 1D transport model. Experiment refers to values obtained/used in experiments. Computed refers to parameters computed, parameters obtained from literature are marked in parentheses.

Notation	Parameter	Numerical value		References
		Liquid	Polymer	
L	Electrolyte thickness (m)	35×10^{-6}		46
$M_{cathode}$	Experimental slurry thickness (m)	40×10^{-06}	32.5×10^{-06}	Experiment
M	Model cathode thickness (m)	3.78×10^{-06}	7.43×10^{-06}	Computed
V_{active}	Active material volume fraction	0.09	0.23	Computed
A	Geometric area of experimental cathode (m^2)	7.85×10^{-05}	2.80×10^{-05}	Experimental
m_l	Active cathode mass loading (mg/cm^2)	1.5	3	Experiment
S_c	1 C specific capacity (mAh/g)	82.82		Experimental
i	Current density normal to the electrode surface (A/m^2) at 1 C	1.25	2.46	Estimation
E_{eq}	OCV of NNFMO	Experimental 0.2 C discharge curve for liquid electrolyte against Na metal		
α_{anode}	Butler Volmer charge transfer coefficient at the anode interface	0.5		13, 14
$\alpha_{cathode}$	Butler Volmer charge transfer coefficient at the cathode interface	0.6		13, 14
C^{+}_{Na0}	Total concentration of Na^+ in the electrolyte (mobile + immobile) (mol/m^3)	1.0×10^{03}	1.1×10^{03}	Experiment
δ	Fraction of mobile Na^+ w.r.t to total Na^+ in the electrolyte	0.9	0.12	Set
C^{+}_{Na}	Concentration of mobile Na^+ in the electrolyte	Variable		
C^{s}_{Na}	Concentration of intercalated Na^+ in the cathode	Variable		
$C^{s}_{Na\,max}$	Maximum concentration of Na^+ in the electrode (mol/m^3)	$2.58 \times 10^{+04}$		Computed from[45]
$C^{s}_{Na\,min}$	Minimum concentration of Na^+ in the electrode (mol/m^3)	$1.29 \times 10^{+04}$		
t^+	Transference number	0.42		Experiment[55,56]
R	Gas Constant (J/mol·K)	8.314		
T	Temperature of operation (K)	300	333	

were cut and then rolled between two mylar sheets to prepare the fresh Na metal electrodes prior to assembly of the coin cells. Cells were annealed at 80 °C for 4 h prior to electrochemical testing. Table 1 summarizes these parameters used in the model.

Results and Discussions

Numerical values of parameters obtained by ML-assistant fitting.—With the cell geometry based on experiments, we simulated the discharge process of Na|PEG-PGMA-NaFSI|NNFMO (solid polymer electrolyte) and Na|EC-DMC-$NaClO_4$|NNFMO (liquid electrolyte setup). As explained in the methods section, we use a Gaussian Process Regressor to fit and evaluate the 5 electrochemical parameters in the case of the liquid electrolyte and 6 parameters for the case of the solid polymer electrolyte. The parameters obtained by fitting for the liquid electrolyte experiment CV at 4 C ($i = 5.0$ A/m^2) (SI Fig. S–2) are provided in Table II. It is interesting to note that the experimental curves for the liquid and polymer electrolytes exhibit qualitative and quantitative differences. Qualitatively, the polymer case for example does not exhibit the phase transitions evident by the shoulders present in the liquid electrolyte case at ∼3 V. Quantitatively, polymer electrolyte exhibits ∼10% lower specific capacity.

The diffusivity of Na in cathode $\boldsymbol{D^s_{Na}}$.—Fitted for the two battery systems is very similar (4.79×10^{-13} m^2/s for liquid and 2.41×10^{-13} m^2/s for polymer solid electrolyte). We believe this lends strong credibility to our model for two reasons. First, this confirms that the solid-state diffusivity is a unique material phenomenon to NNFMO and hence does not change with the electrolyte that has been considered. Second, the value is in line with the values reported in literature 5×10^{-12} m^2/s,[39] 1×10^{-12} m^2/s,[38] 2×10^{-11} m^2/s,[68] and 9×10^{-13} m^2/s.[60]

The fitted diffusivity of Na^+ *in electrolyte.—*D^+_{Na} is 3.49×10^{-11} m^2/s for liquid and 4.8510^{-11} m^2/s for the polymer electrolyte, respectively. While the diffusivity is similar, the fraction of mobile Na^+ is 0.9 in the liquid electrolyte and only 0.12 in the solid electrolyte, leading to the difference in the ionic conductivity.

Table II. Parameters obtained from fitting models to experiments.

Notation	Parameter	Optimized parameters	
		Liquid	Polymer
k_r	Sodium recombination rate at the anode-electrolyte interface ($m^3/mol·s$)	2.38×10^{-06}	0.52
D^s_{Na}	Diffusivity of Na in the cathode (m^2/s)	4.79×10^{-13}	2.41×10^{-13}
D^+_{Na}	Diffusivity of Na^+ in electrolyte (m^2/s)	3.49×10^{-11}	4.85×10^{-11}
k_{pos}	Charge transfer coefficient cathode ($mol/m^2·s$)	7.62×10^{-06}	4.99×10^{-04}
k_{neg}	Charge transfer coefficient anode ($mol/m^2·s$)	2.94×10^{-03}	1.10×10^{-05}
γ	Contact Area	1 (assumed)	0.82

The liquid electrolyte cell was tested at 300 K while the SPE cell was at 333 K. This is commensurate with the trend seen in literature where Na^+ diffusivity in a liquid medium is reported in the range of 10^{-10} m^2/s to 10^{-11} m^2/s[40,41] while some report as low as 10^{-13} m^2/s.[42] For the polymer electrolyte, the predicted Na^+ diffusivity at 60°C is aligned with literature reported values of 10^{-11} to 10^{-13} m^2/s.[23,43,69,70] It is interesting to note that for both the liquid and the polymer-based electrolyte, the diffusivity is about two orders of magnitude higher than the solid-state diffusivity of Na in NNFMO. The ionic conductivity (σ) of the two types of electrolytes may be estimated as $\sim\frac{F^2}{RT}C^+_{Na0}D^+_{Na}\delta$. The σ is estimated to be around 1.17×10^{-3} S/cm[1] and 0.22×10^{-3} S/cm for the liquid and the SPE, respectively, within the typically reported ranges in literature. Using these ion conductivities to estimate the voltage drop in the electrolytes by $\sim\frac{iL}{\sigma}$, leads to a voltage drop of ~0.4 mV and ~3 mV for a 35 and 260-micron thick liquid electrolyte, respectively at the corresponding 1 C rate (i = 1.25A/m^2). For the SPE, a 35-micron thick SPE electrolyte will lead to a voltage drop of ~2 mV. Thus, increasing the liquid electrolyte thickness from 35 microns to 670 microns shows negligible changes in the discharge curve (Fig. S–3 in SI), validating the choice of electrolyte thickness used in the model.

The liquid electrolyte used in this work has a concentration of 1 M of salt, which is within the dilute limit. While the concentration assumption holds in the bulk region, it needs an investigation at the interface between the anode and the electrolyte. This can be verified by calculating the change in the concentration upon discharge of the 1 nm region near the interface into the electrolyte in a characteristic diffusion time ($t \sim x^2/D^+_{Na}$) at 1 A/m^2 current density. In the strictest limiting case, we also consider that the Na^+ ions do not diffuse out of the 1 nm box. It was found that the change in concentration in the electrolyte is $< 1\%$, thus our model stays in the dilute range throughout the operation. However, at higher current densities of ~10 A/m^2, this assumption is no longer valid, and we see deviations between the experimental and the modeling predicted discharge curves.

The rate constant k_r is the rate for Na^+ becoming immobile; k_d is the rate for the immobile ions becoming mobile again. They are related to the mobile ion concentration, as $\frac{k_d}{k_r} = C_{Na}{}_t{}^+\frac{\delta^2}{1-\delta}$. In our analysis, the δ for liquid electrolyte was set to 0.9, and the SPE was set to 0.12. The fit value for the k_r for liquid electrolyte is 2.38×10^{-06} and SPE is 0.52 m^3/mol·s, the rate at which the Na^+ is immobilized in the liquid electrolyte is much lower than the SPE.

The charge transfer rate constants $\boldsymbol{k_{pos}}$ *and* $\boldsymbol{k_{neg}}$ *at both the electrode|electrolyte.*—The cathode|electrolyte rate constant for the liquid electrolyte is 7.62×10^{-06} mol/m^2s and is 4.99×10^{-04} mol/m^2s for SPE. This reflects that the charge transfer reaction rate may primarily be dictated by the cathode type, for example, composite cathode with polymer infiltration. For the case of the charge transfer reaction rate at the anode|electrolyte interface, the liquid and the polymer electrolyte gave different values. The fit value for the liquid electrolyte is 2.94×10^{-03} mol/m^2·s while for the SPE, it is 1.10×10^{-05} mol/m^2·s. This may be because of two possible reasons, first is the different nature of solid electrolyte interface (SEI) formed in liquid vs polymer electrolyte for the same anode.[71] Secondly, the void and imperfect contact created at the Na-solid electrolyte interface during stripping dramatically increase the interface impedance while the Na-liquid electrolyte interface remained conformal during discharge. In this model, the contact area at the anode|electrolyte interface is treated as perfect contact.

The contact area fraction γ at the cathode|electrolyte interface was fitted. For the case of the SPE, our fitting model provides a value of contact area factor of 0.82. This means that only ~80% of the cathode is in intimate electrochemical contact with the electrolyte. The low value of the contact fraction may explain the low capacity obtained by the polymer electrolyte experimental discharge curve when compared to the liquid electrolyte. On the other hand, we assume 100% infiltration of pores by liquid and hence a contact area fraction of 1.

Simulated discharge curves for the liquid electrolyte case.—The parameter fitting for the liquid electrolyte used the experiment CV conducted at 4 C (i = 5.0 A/m^2). The optimized parameters listed in Table II are then used as inputs to obtain discharge curves at different C rates from the COMSOL model, as shown in Fig. 2. The black line curves are for the experimentally obtained discharge curve. The green dotted curves represent the curves obtained from the model. It is evident that the fitting parameters obtained for fitting the 4 C discharge curves show excellent agreement with the discharge curves at other rates.

Simulated discharge curves for the polymer electrolyte case.—To understand the generalizability of our model, the discharge curve obtained from the liquid electrolyte case at 0.2 C is used as the OCV for the battery system containing SPE (Fig. S–4 in SI). The hypothesis is that a generalizable model should predict an accurate fit for the experiment, independent of electrolytes. To verify this, the experimental solid polymer electrolyte case was discharged at 0.2 C (0.5 A m^{-2}). The fitting was hence only conducted using a 0.2 C dataset. The fit parameters, when used in COMSOL, yield the dotted orange curve shown in Fig. 3, which is compared to the experimentally obtained curve shown in the solid red line.

The RMS obtained for this fit is 3.56 mAh/g[1] (within 5% of the maximum experimentally obtained specific capacity). The curve shows all the matching trends except for the shoulder at 2.85 V which is seen in the modeling curve but unseen in the experimental curve. This behavior is analogous to the peak shift due to active material loss during battery aging. It can be derived for a full battery that, parallel shift peaks (no distance change) on the dV/dQ vs Q curves represent active sodium (lithium) amount loss, while the shortening peak separation indicates the loss of active materials to host sodium(lithium).[72] Motivated by this observation, a total scaling factor of 0.91 was multiplied by the specific capacity at each voltage to mimic the loss of active cathode material. This produces the curve shown in pink which has an RMS of 1.97 mAh/g[1] (within 2.8% of the experimentally obtained specific capacity). This scaling factor represents that not all of the active material in the cathode is "sodiating." We believe that the contact area loss parameter and this inefficiency factor are related, however, in the case of a 1D diffusion model, it is not straightforward to establish an analytical relationship. Nonetheless, we show that a simple physics inspired scaling factor not only leads to capturing the qualitative aspects of the experimental discharge curve, but also leads to accurate prediction of quantitative discharge capacity and RMS error.

Thus, our model accurately predicts the discharge behavior of the 1D battery suitable for the tested electrolyte and the cathode architecture. This model can hence be used to predict the discharge behavior of electrochemically active materials at the continuum scale.

Predicting cathode thickness, utilization, overpotentials during battery discharge.—One direct application of our model is its ability to guide experiments and help in predictive modeling. We investigate the effect of increasing the thickness of the cathode and commensurately increasing the current density. To investigate this, we chose the SPE as the electrolyte medium because the hierarchical batteries will be infiltrated by a solid electrolyte. The analysis is done as follows. In the first step, the thickness of the cathode is varied from 1 to 25 microns while holding the SPE thickness constant at 35 microns and the C-rate is held constant at 0.5 C. The current density scales with the thickness of the cathode linearly (e.g. 0.5 C corresponding to i = 0.166 A/m^2 for 1-micron thick cathode and i = 4.15 A/m^2 for a 25-micron thick cathode). In the second

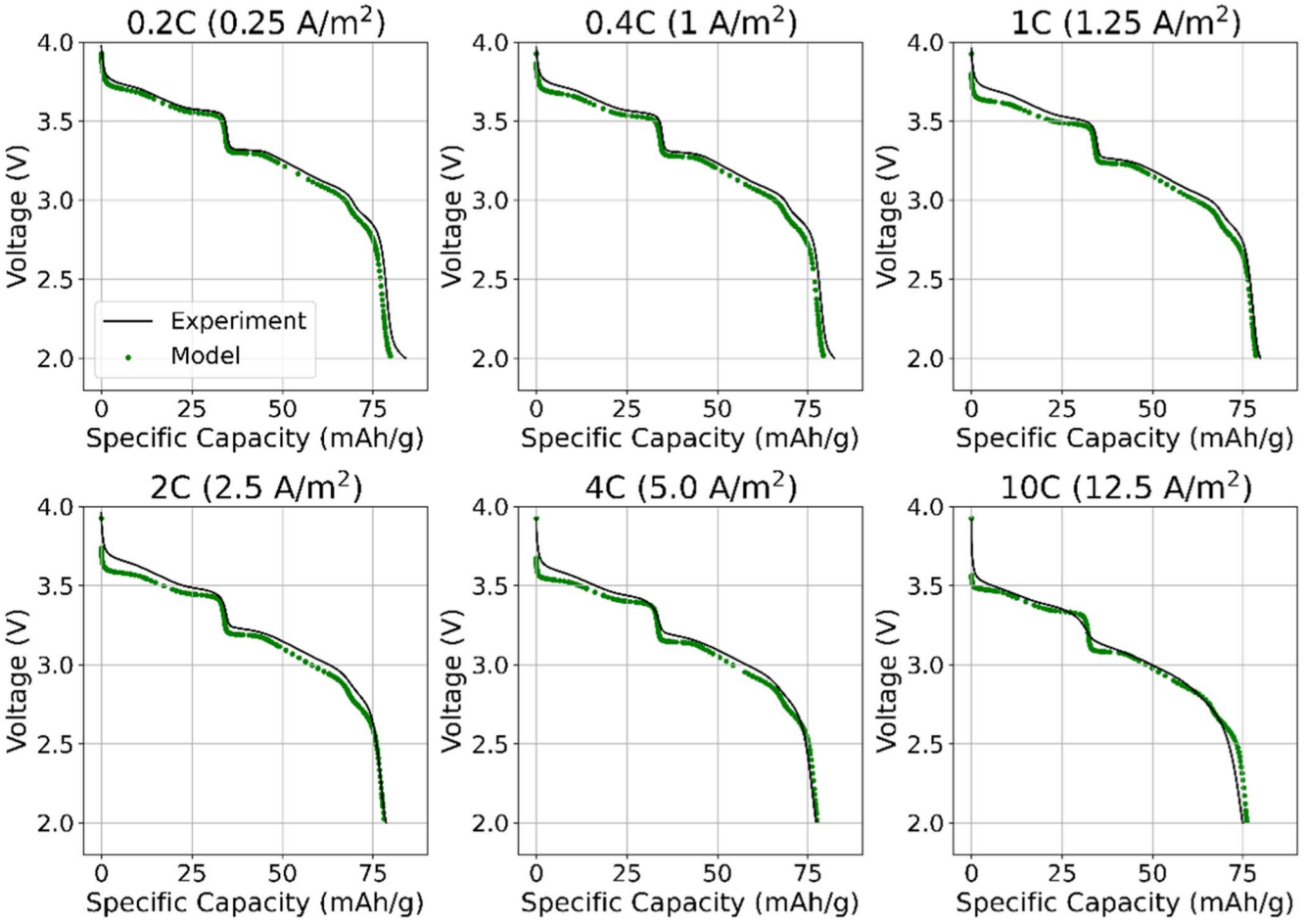

Figure 2. Comparison of discharge curves obtained for the liquid electrolytes experimental vs model at various C rates (0.2, 0.4, 1, 2, 4, 10 C) black solid lines are for the experiment, green dotted curve is for the model. The green model curves were obtained using parameters that are fit using a 4 C (5.0 A/m^2) dataset.

step, the thickness of the SPE is varied from 2 microns to 45 microns while the thickness of the electrode is held constant at 10 microns and the current density at 1.66 A/m^2 corresponds to 0.5 C (Fig. S–5 in SI). It is noted for both studies, the parameters used correspond to the SPE cells.

The results for the variation in cathode thickness (with constant electrolyte thickness and C rate) are shown in Fig. 4, with the discharge curves (Fig. 4a) and the sodiation extent vs the normalized length of the cathodes of different thicknesses (Fig. 4b). It can be seen from Fig. 4a, that increasing the thickness of the cathode at constant C causes a downward shift in the discharge curve. Another observation is the decrease in the specific capacity obtained due to the increasing thickness of the cathode (10% decrease at 25 microns (purple curve) when benchmarked against 1-micron thickness (navy curve).

Theoretically, the utilization rate of the cathode can be analytically linked to the current density and the thickness of the electrode.[12] Setting a utilization rate of 80% as the criteria, we obtain an upper bound for solid state diffusion limited length of cathode M$\sim$32 microns. This is consistent with the Na concentration profile in the scaled cathode thickness in Fig. 4b. At a thickness less than 10 microns, the utilization rate is almost 100%. At around $\sim$25-micron cathode thickness, the utilization rate drops to 92% (corresponding to x = 0.61 in $Na_{0.66}$NFMO) corroborating the drop in specific capacity as shown in Fig. 4a. Hence, the cathode utilization up to 25 micron thickness cannot explain the voltage drop seen in Fig. 4a.

Next, we discuss the overpotential contributions to the cell discharge voltage (V^*) drop from its open circuit voltage E_{eq}, shown in Fig. 4a.

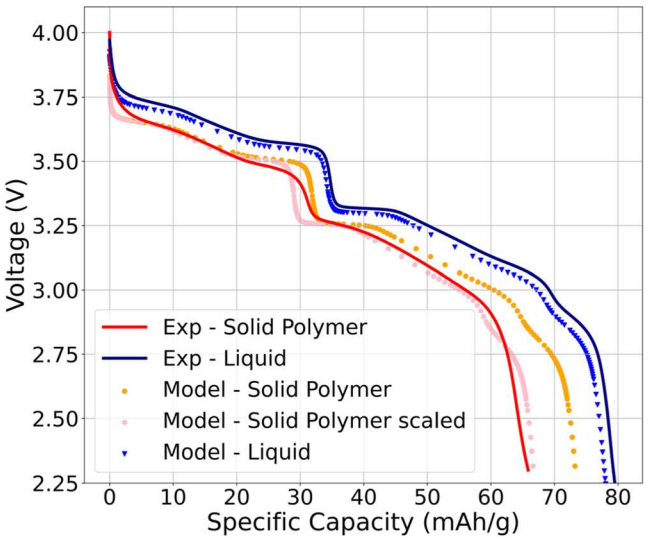

Figure 3. Comparison of the experimentally and model obtained discharge curves at respective 0.2C rates (0.25 A/m^2 for liquid & 0.50 A/m^2 for SPE). Solid lines show experimentally obtained curves, navy for liquid electrolyte, red for the SPE. Dotted lines represent modelling curve. The orange dots show discharge curve using the SPE parameters, the pink dots represent the discharge curve for SPE with a scaling factor of 0.91 multiplied to the specific capacity (with Voltage as is). The blue triangles represent the model liquid electrolyte discharge curve. The model curves for liquid electrolyte was generated by using parameters obtained from fitting a 4C (5.0 A/m^2) dataset, while the model curves obtained for the SPE was generated by using parameters obtained from fitting a 0.2C (0.5 A/m^2) dataset.

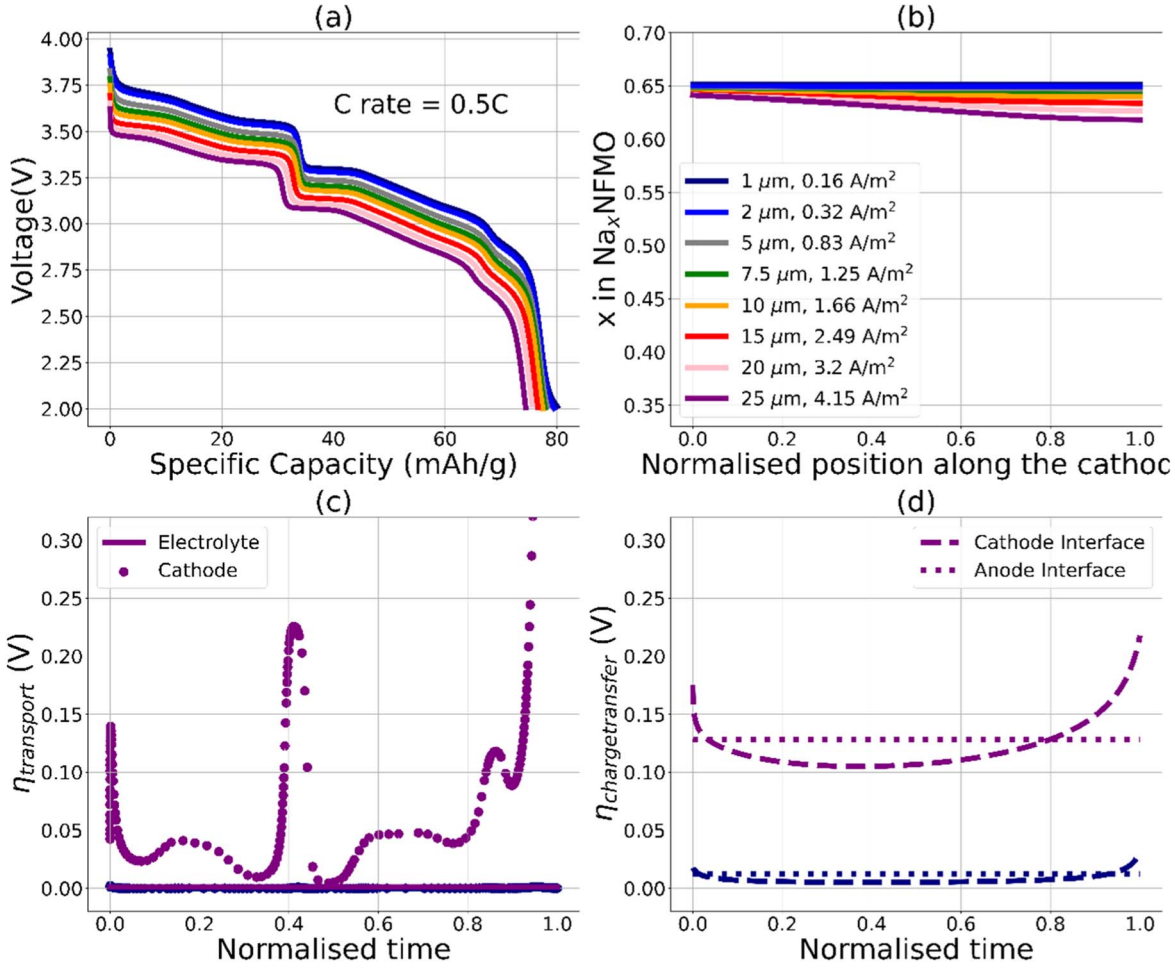

Figure 4. Investigation of the effect of increasing the thickness of the cathode at a constant 0.5 C rate on the CV curves obtained for the SPE parameters, the thickness of the cathode and the current density used in the simulation are provided in the legend of the top right figure. (a) Shows the modeled discharge behavior of various thicknesses of cathode for the SPE at 0.5 C current. (b) Shows the utilization of the active cathode material along the normalized length of the cathode for various thicknesses at the end of the discharge. (c) The time evolution of the overpotential contribution from mass transport effects. (d) The time evolution of the overpotential contributions from the charge transfer at the interfaces. The dashed line is from the overpotential from the electrolyte|cathode interface and the dotted line is from the anode|electrolyte interface. Purple color is for a 25-micron thickness cathode (4.15 A/m^2), and navy is for a 1-micron thickness cathode (0.16 A/m^2).

$$V^* = E_{eq} - \eta_{cathode} - \eta_{electrolyte} - \eta_{ct}^{anode|electrolyte} - \eta_{ct}^{electrolyte|cathode} \quad [10]$$

where $\eta_{cathode}$ is the mass transport overpotential in the cathode. $\eta_{electrolyte}$ is the mass transport overpotential in the electrolyte. η_{ct}^{anode} is the charge transfer overpotential at the anode|electrolyte interface and $\eta_{ct}^{cathode}$ from the electrolyte|cathode interface in the Butler Volmer equation (Eq. 7 and 1 respectively). Figure 4c shows the COMSOL computed temporal evolution of the overpotentials $\eta_{cathode}$ (dots) and $\eta_{electrolyte}$ (solid lines) for the case of 1-micron (navy) and 25-micron cathode thickness (purple) cases with time. Figure 4d shows the COMSOL computed overpotentials due to charge transfer, dashed lines for $\eta_{ct}^{electrolyte|cathode}$ and dotted line for $\eta_{ct}^{anode|electrolyte}$. In both cases, these overpotentials for the 1-micron thickness cathode are negligible. For the case of 25-micron thickness, all overpotentials increase proportionally to the current density which increases 25 times due to the constant C-rate used, e.g. i = 0.16 A/m^2 vs i = 4.15 A/m^2) for the 1 and 25-micron thickness cathode, respectively.

The overpotentials of $\eta_{electrolyte}$, (Fig. 4c), $\eta_{ct}^{anode|electrolyte}$ (Fig. 4d) for the 25-micron thick cathode are almost constant over time. $\eta_{ct}^{electrolyte|cathode}$ for the case of 25 microns is almost constant over its course of time, however rises by the end of the discharge as the difference in the concentration term in Eq. 7($C_{Na|\max}^{s} - C_{Na}^{s}$) drops to zero. On the other hand, the $\eta_{cathode}$ showed a peak value around the region when the sodiation of NNFMO goes through a vertical drop in OCV. This is because the numerical solution of the mass transport overpotential in the cathode is proportional to the slope of the OCV, hence showing the sharp increase during the transition from single to 2-phase region of NNFMO (when the slope increases suddenly). Since $\eta_{ct}^{anode|electrolyte} + \eta_{ct}^{electrolyte|cathode}$ is about five times larger than $\eta_{electrolyte}$, the overall overpotentials are dominated by the charge transfer except during the phase transition peak, within which the $\eta_{cathode}$ also has a strong contribution.

Hence, increasing the thickness of the cathode and commensurately increasing the current density at the same C rate will lead to overpotentials which arise primarily from charge transfer at the interfaces. With simplified Tafel equations, we provide an analytical equation (details in SI) which can be used to approximate the total

charge transfer overpotential (from both interfaces) η_{ct}^{Total}, based on the C rate and the thickness of the cathode.

$$\eta_{ct}^{Total} = (A_c + A_a)\log_{10}[C_{rate}{\cdot}S_c{\cdot}C_{Na\,\max}^{s}{\cdot}M_w{\cdot}M] - (A_c\log_{10}[i_{0\,pos}] + A_a\log_{10}[i_{0\,neg}]) \quad [11]$$

where $i_{0\,pos}$, i_{0neg} are the exchange current densities (A/m^2); A_c and A_a are the Tafel slopes (V) at the cathode and anode interface respectively; and the specific capacity S_c (mAh), Molecular Weight M_w (g) and the thickness of cathode M can be inserted in meters. Equation 11 can be used to estimate the η_{ct}^{Total} based on the M and the C rate or vice versa. One way to estimate an upper limit of the η_{ct}^{Total} is by analyzing the energy density of the cathode which is the area under the discharge curve. For an equilibrium discharge curve, the energy density of the cathode obtained is 275.6 Wh kg^{-1}. Ignoring the effect of utilization, a total overpotential of 0.23 V causes a 10% drop in the energy density of the cathode by shifting the curve downward. Further assuming only η_{ct}^{Total} to be the dominant overpotential gives an upper limit of 0.23 V and a corresponding current density of ~3.07 A m^{-2}. Assuming a C rate of 0.5, this corresponds to a thickness of 18.5 microns for the cathode.

As the majority of the overpotential was contributed by the charge transfer process, the sensitivity to the thickness of the electrolyte is low (shown in SI) within these testing conditions. Furthermore, the diffusivity of Na^+ in the electrolyte is an order of magnitude higher than the solid-state diffusivity of Na in the cathode, hence mass transport overpotential in the electrolyte is also lower than in the cathode. A full analysis incorporating the density of the electrolyte, shape effects of the active material, and electrolyte and finite sized anodes will be done in a follow-up article on 3D hierarchical batteries.

Conclusions

Hierarchical solid-state sodium ion batteries offer the possibility to improve energy density while being more equitable and sustainable. Continuum scale models can shorten the design process of these upcoming battery technologies. However, these models require rich experimental input which may not exist in these upcoming systems. The input parameters for these systems can be obtained using a surrogate model which requires minimum experimental input (coin cell). We first developed a 1D model of electrochemical discharge in COMSOL and the parameters for the model were obtained using a surrogate model. The surrogate model accurately evaluated electrochemical parameters like diffusivity, rate constants of charge transfer reactions at the electrode|electrolyte interfaces, and contact area loss. We also showed that our parameter fitting procedure and the continuum model are independent of the choice of electrolyte viz liquid, solid polymer. The average of the surrogate model predicted diffusivity of the Na in the NNFMO cathode medium is not strongly dependent on the electrolyte (2.10×10^{-13} m^2/s). It is in the lower range of reported values in the literature, maybe due to the 1D simplification. Furthermore, the model predicted the Na^+ diffusivity in the polymer (4.85×10^{-11} m^2/s) is faster than that in liquid electrolyte (3.49×10^{-11} m^2/s). However, this difference is much less than the typical experimental values. The rate constants of the charge transfer reaction at the electrolyte|cathode interface are similar, showing that the rate constant at the cathode end is dictated by the cathode material chemistry and processing. The optimized parameters predicted by the surrogate model were used as input parameters for a 1D continuum model. The 1D continuum model was used to understand the effect of scaling the thickness of the cathode material on the discharge curve at a constant 0.5 C rate. Two major trends were observed, the high utilization rate of the cathode and large potential drops. The source of the potential drops was found to be the penalizing charge transfer overpotentials at high current densities. An analytical model was derived to predict the optimal cathode thickness for a given current C rate.

Acknowledgments

This work is supported by the National Science Foundation under grant DMR-2134715.

ORCID

Christopher Y. Li https://orcid.org/0000-0003-2431-7099
Eric Detsi https://orcid.org/0000-0002-4009-7260
Yue Qi https://orcid.org/0000-0001-5331-1193

References

1. B. D. Jeffrey, W. Long, D. R. Rolison, and H. S. White, *Chem. Rev.*, **104**, 4463 (2004).
2. M. Roberts et al., *J. Mater. Chem.*, **21**, 9876 (2011).
3. A. Pearse, T. Schmitt, E. Sahadeo, D. M. Stewart, A. Kozen, K. Gerasopoulos, A. A. Talin, S. B. Lee, G. W. Rubloff, and K. E. Gregorczyk, *ACS Nano*, **12**, 4286 (2018).
4. A. A. Talin, D. Ruzmetov, A. Kolmakov, K. McKelvey, N. Ware, F. El Gabaly, B. Dunn, and H. S. White, *ACS Appl. Mater. Interfaces*, **8**, 32385 (2016).
5. S. Lobe, A. Bauer, S. Uhlenbruck, and D. Fattakhova-Rohlfing, *Adv. Sci.*, **8**, 2002044 (2021).
6. K.-H. Chen et al., *Journal of Power Sources*, **471**, 228475 (2020).
7. R. Dubey, M. D. Zwahlen, Y. Shynkarenko, S. Yakunin, A. Fuerst, M. V. Kovalenko, and K. V. Kravchyk, *Batteries & Supercaps*, **4**, 464 (2020).
8. G. Du, Y. Zhou, X. Tian, G. Wu, Y. Xi, and S. Zhao, *Applied Surface Science*, **453**, 493 (2018).
9. B. Delattre, R. Amin, J. Sander, J. De Coninck, A. P. Tomsia, and Y.-M. Chiang, *J. Electrochem. Soc.*, **165**, A388 (2018).
10. B. D. McCloskey, *J. Phys. Chem. Lett.*, **6**, 4581 (2015).
11. C. Heubner, M. Schneider, and A. Michaelis, *Adv. Energy Mater.*, **10**, 1 (2020).
12. M. Weiss et al., *Adv. Energy Mater.*, **11**, 1 (2021).
13. D. Danilov, R. A. H. Niessen, and P. H. L. Notten, *J. Electrochem. Soc.*, **158**, A215 (2011).
14. H.-K. Tian and Y. Qi, *J. Electrochem. Soc.*, **164**, E3512 (2017).
15. F. Wang and M. Tang, *Cell Reports Physical Science*, **1**, 100192 (2020).
16. M. Doyle, T. F. Fuller, and J. Newman, *J. Electrochem. Soc.*, **140**, 1526 (1993).
17. T. F. Fuller, M. Doyle, and J. Newman, *J. Electrochem. Soc.*, **141**, 1 (1994).
18. M. Guo, G. Sikha, and R. E. White, *J. Electrochem. Soc.*, **158**, A122 (2011).
19. G. Ning and B. N. Popov, *J. Electrochem. Soc.*, **151**, A1584 (2004).
20. S. Santhanagopalan, Q. Guo, P. Ramadass, and R. E. White, *Journal of Power Sources*, **156**, 620 (2006).
21. H.-K. Tian, A. Chakraborty, A. A. Talin, P. Eisenlohr, and Y. Qi, *J. Electrochem. Soc.*, **167**, 090541 (2020).
22. J. Christensen, *J. Electrochem. Soc.*, **157**, A366 (2010).
23. H.-K. Kim, N. P. Balsara, and V. Srinivasan, *J. Electrochem. Soc.*, **167**, 110559 (2020).
24. N. Yabuuchi, K. Kubota, M. Dahbi, and S. Komaba, *Chem. Rev.*, **114**, 11636 (2014).
25. S.-W. Kim, D.-H. Seo, X. Ma, G. Ceder, and K. Kang, *Adv. Energy Mater.*, **2**, 710 (2012).
26. C. Vaalma, D. Buchholz, M. Weil, and S. Passerini, *Nature Review Materials*, **3**, 18013 (2018).
27. S. T. Dix, J. S. Lowe, M. R. Avei, and T. R. Garrick, *J. Electrochem. Soc.*, **170**, 083503 (2023).
28. Z. Khalik, M. C.-F. Donkers, J. Sturm, and H. J. Bergveld, *Journal of Power Sources*, **499**, 229901 (2021).
29. M. Streb, M. Andersson, V. Löfqvist Klass, M. Klett, M. Johansson, and G. Lindbergh, *eTransportation*, **16**, 100231 (2023).
30. S. Kim, S. Kim, Y. Y. Choi, and J.-I. Choi, *Journal of Energy Storage*, **71**, 108129 (2023).
31. S. Kohtz, Y. Xu, Z. Zheng, and P. Wang, *Mechanical Systems and Signal Processing*, **172**, 109002 (2022).
32. R. Alizadeh, J. K. Allen, and F. Mistree, *Res. Eng. Des.*, **31**, 275 (2020).
33. A. Bhosekar and M. Ierapetritou, *Computers and Chemical Engineering*, **108**, 250 (2018).
34. N. Dawson-Elli, S. B. Lee, M. Pathak, K. Mitra, and V. R. Subramanian, *J. Electrochem. Soc.*, **165**, A1 (2018).
35. M. Quartulli, A. Gil, A. M. Florez-Tapia, P. Cereijo, E. Ayerbe, and I. G. Olaizola, *Energies*, **14**, 4115 (2021).
36. Y. Zhou, B.-C. Wang, H.-X. Li, H.-D. Yang, and Z. Liu, *IEEE Transactions on Industrial Informatics*, **17**, 5909 (2021).
37. Z.-Y. Shui, X.-H. Li, Y. Feng, B.-C. Wang, and Y. Wang, *IEEE Transactions on Industrial Electronics*, **70**, 1521 (2023).
38. T. Chen, W. Liu, Y. Zhuo, H. Hu, M. Zhu, R. Cai, X. Chen, J. Yan, and K. Liu, *Journal of Energy Chemistry*, **43**, 148 (2020).
39. F. Fu, P. Liu, and H. Wang, *Materials Letters*, **253**, 124 (2019).
40. J. Landesfeind, T. Hosaka, M. Graf, K. Kubota, S. Komaba, and H. A. Gasteiger, *J. Electrochem. Soc.*, **168**, 040538 (2021).

41. D. Morales, R. E. Ruther, J. Nanda, and S. Greenbaum, *Electrochim. Acta*, **304**, 239 (2019).
42. J. Fogeling, M. Kunze, M. Schonhoff, and N. A. Stolwijk, *Phys. Chem. Chem. Phys.*, **12**, 7148 (2010).
43. Y. Ma, M. Doyle, T. F. Fuller, M. M. Doeff, L. C. De Jonghe, and J. Newman, *J. Electrochem. Soc.*, **142**, 1859 (1995).
44. K.-H. Shen and L. M. Hall, *Macromolecules*, **53**, 10086 (2020).
45. D. Pahari and S. Puravankara, *Journal of Power Sources*, **455**, 227957 (2020).
46. D. Djian, F. Alloin, S. Martinet, H. Lignier, and J. Y. Sanchez, *Journal of Power Sources*, **172**, 416 (2007).
47. C.-W. Wang and A. M. Sastry, *J. Electrochem. Soc.*, **154**, A1035 (2007).
48. A. Ehrl, J. Landesfeind, W. A. Wall, and H. A. Gasteiger, *J. Electrochem. Soc.*, **164**, A826 (2017).
49. C. A. C. Sequeira and A. Hooper, *Solid State Ionics*, **9**, 1131 (1983).
50. T. Dev, J. L. Schaefer, and A. Salvadori, *Journal of Energy Storage*, **68**, 107581 (2023).
51. L. H.-J. Raijmakers, D. L. Danilov, R. A. Eichel, and P. H.-L. Notten, *Electrochim. Acta*, **330**, 135147 (2020).
52. L. O. Valøena and J. N. Reimers, *J. Electrochem. Soc.*, **152**, A882 (2005).
53. R. Singh, C. Maheshwaran, D. K. Kanchan, K. Mishra, P. K. Singh, and D. Kumar, *Journal of Molecular Liquids*, **336**, 116594 (2021).
54. A. K. Chauhan, D. Kumar, K. Mishra, and A. Singh, *Materials Today Communications*, **26**, 101713 (2021).
55. K. Biernacka, J. Sun, F. Makhlooghiazad, A. Balkis, I. E. Gunathilaka, L. A. O'Dell, M. G. Mestres, P. C. Howlett, J. M. Pringle, and M. Forsyth, *J. Phys.: Energy*, **5**, 014006 (2022).
56. K. Sirengo, A. Babu, B. Brennan, and S. C. Pillai, *Journal of Energy Chemistry*, **81**, 321 (2023).
57. M. H. Han, E. Gonzalo, G. Singh, and T. Rojo, *Energy Environ. Sci.*, **8**, 81 (2015).
58. D. H. Lee, J. Xu, and Y. S. Meng, *Phys. Chem. Chem. Phys.*, **15**, 3304 (2013).
59. A. Gutierrez, W. M. Dose, O. Borkiewicz, F. Guo, M. Avdeev, S. Kim, T. T. Fister, Y. Ren, J. Bareño, and C. S. Johnson, *The Journal of Physical Chemistry C*, **122**, 23251 (2018).
60. Y. Zhang, M. Wu, J. Ma, G. Wei, Y. Ling, R. Zhang, and Y. Huang, *ACS Cent Sci*, **6**, 232 (2020).
61. Q. Liu, Z. Hu, M. Chen, C. Zou, H. Jin, S. Wang, Q. Gu, and S. Chou, *J. Mater. Chem. A*, **7**, 9215 (2019).
62. COMSOL Multiphysics® v. 5.6. www.comsol.com. COMSOL AB, Stockholm, Sweden.
63. F. Pedregosa et al., *Journal of Machine Learning Research*, **12**, 2825 (2011).
64. O. Ruiz, M. Cochrane, M. Li, Y. Yan, K. Ma, J. Fu, Z. Wang, S. H. Tolbert, V. B. Shenoy, and E. Detsi, *Adv. Energy Mater.*, **8**, 1801781 (2018).
65. E. Detsi, J. B. Cook, B. Lesel, C. Turner, Y. L. Liang, S. Robbennolt, and S. H. Tolbert, *Energy Environ. Sci.*, **9**, 540 (2016).
66. S. Y. Lee, J. H. Kim, and Y. C. Kang, *Electrochim. Acta*, **225**, 86 (2017).
67. Y. Liu, X. Fang, A. Zhang, C. Shen, Q. Liu, H. A. Enaya, and C. Zhou, *Nano Energy*, **27**, 27 (2016).
68. B. Peng, Z. Sun, L. Zhao, S. Zeng, and G. Zhang, *Batteries & Supercaps*, **4**, 456 (2020).
69. A. Ferry, M. M. Doeff, and L. C. DeJonghe, *Electrochim. Acta*, **43**, 1387 (1998).
70. D. M. Pesko, K. Timachova, R. Bhattacharya, M. C. Smith, I. Villaluenga, J. Newman, and N. P. Balsara, *J. Electrochem. Soc.*, **164**, E3569 (2017).
71. N. Takenaka, Y. Suzuki, H. Sakai, and M. Nagaoka, *The Journal of Physical Chemistry C*, **118**, 10874 (2014).
72. P. Liu, J. Wang, J. Hicks-Garner, E. Sherman, S. Soukiazian, M. Verbrugge, H. Tataria, J. Musser, and P. Finamorec, *J. Electrochem. Soc.*, **157**, A499 (2010).